Chemistry and Materials Research
ISSN 2224- 3224 (Print) ISSN 2225- 0956 (Online)
Vol.6 No.12, 2014

Spray Freeze Drying as a Smart Method in Preparation of Ultra-Fine CeO_2-MO_X Materials

Dalia R. Abd El-Hafiz (Corresponding author)
Egyptian Petroleum Research Institute, Cairo, 11727, Egypt
E-mail: dalia_epri@yahoo.com

Mohamed A. Ebiad and Lamia. S. Mohamed
Egyptian Petroleum Research Institute, Cairo, 11727, Egypt
m_a_ebaad@yahoo.com and lamiakaid@yahoo.com

Abstract
Cerium-oxide based nano-materials attract increasing interest for their use in multiple applications. In particular, the substitution of Ce atoms by other elements with lower or higher oxidation state is used to control oxygen vacancies within the oxide structures, which can greatly enhance the material properties for catalysis applications. Among the synthesis approaches, spray freeze drying method has been proved to be an extremely efficient method for the preparation of uniform nano-partical for different application. In this method, the pure solution or mixed solutions were directly sprayed into liquid nitrogen and immediately frozen to form a suspension, then, the iced droplets were dried in the freeze-dryer to reach the final product. However, in this work we deal with, the preparation of ultra-fine materials based on CeO_2 fluorite structures and the substitution in its lattice with La and/or Co metal. The effect of Ce/La ratio on the properties of the final product was also investigated. During the experiment, the advantage of spray-freeze-drying process was successfully achieved. The characterization of the powder product was analyzed by means of EDX, TGA, XRD, DLS, and TEM which confirm the formation of nano-particles in the fluorite structure. For Ce:Co and when the Ce: La ratio is 0.2, 0.5, only cubic phase of CeO_2-MO_2 solid solution with fluorite structure is observed with hig oxygen storage capacity, while Ce-La_1 show the hcp structure of lanthanum.
Keywords: nano-materials, Ceria, Lanthanium, metal loading spray freeze drying

1. Introduction

Over the past decades, cerium oxide based materials (pure or substituted) have been intensively studied as they have been proven to be effective materials in a wide range of applications including catalysis, as three-way samples to control auto-mobile exhaust, adsorpent, oxygen storage, polishing, optics or biomedicine [1-6]. The fluorite structure of ceria oxides have face-centered-cubic (FCC) crystal structure in which each tetravalent metal ion is surrounded by eight equivalent nearest O^{2-} ions forming the vertices of a cube. CeO_2 has excellent redox properties due to the easy reduction of Ce^{+4} to Ce^{+3} associated to the formation of surface oxygen vacancies in the crystalline lattice. Oxygen vacancies are also created when a fluorite oxide is doped by divalent or trivalent impurity ions. Thus, the fluorite oxides have been extensively studied as oxygen ion-conducing materials, due to their high oxygen vacancy concentration and mobility properties. In the catalysis field, fluorite oxides have been explored recently as samples for the oxidation of carbon monoxide and methane. Cerium oxide, associated with other metal oxides, is shown to promote oxygen storage and release, enhance oxygen mobility, form surface/bulk oxygen vacancies, and improve the redox properties of the materials [7, 8].

During the past few years, attention has been paid to surface reaction of Ce−La material [9, 10]. The motivation for these works came from the different application of this material as catalysts, adsorpents or in electronic promotion of the 4f electrons to the 5d conduction band. The doping of La into CeO_2 could decrease the particle size, inhibit the sintering and increase the reducibility of CeO_2 [11]. Bueno-Lopez et al. [12] proved that La^{3+} inserted into the lattice of fluorite structure to form the solid solution, and the reduction temperature of CeO_2 decreased. Belliere et al. [13] revealed that the La enrichment at the surface of cerium–lanthanum solid solutions was an averaged effect and that the occurrence of segregation in a mixed oxide phase was observed by using electron energy-loss spectroscopy in combination with scanning transmission electron microscopy. This segregation did occur within a crystalline particle, where the dopant-rich phase was located at the surface of the dopant-deficient phase.

However, the generally high calcination temperature of the materials during the preparation leads to large grain size and reduces the specific surface area [14], so, the potential applications of these materials are limited. Therefore, in order to increase the specific surface area, the synthesis at a lower temperature would be required. Many studies have been conducted to increase the specific surface area via the various preparation methods such as evaporation drying method using citrate precursor [15], firing method using polyacrylate precursor [16], drip pyrolysis method [17], and spray-freezing/freeze-drying method using nitrate precursor [18]. Most of the applications seek for synthesis processes displaying high reproducibility and advanced control over

the material characteristics, physicochemical properties and composition.

Among those processes, spray freeze drying method demonstrated their efficiency for the synthesis of ultra-fine nano particles, the solution is first sprayed frozen, then vacuum dried at a low temperature and low pressure and finally thermal decomposition the salt in an appropriate atmosphere is carried out to obtain ultra-fine powder [19]. Several works have used spray freeze drying method in the preparation of different ultra-fine metal powders [20], super-conducting materials [21], ultra-fine ceramics [22], high-energy batteries [23], and catalytic materials [24, 25].

This technique has several advantages compared to the conventional method which are prospective for many applications. It is simple, economic, continuous, and rapid process that is compatible with various materials to produce high-purity product [26, 27]. Furthermore, this method produces spherical particles with controllable size that are agglomeration-free and promotes uniform drying to produce a relatively mono-dispersed size, also the removal of ice in small droplets makes the porous structure which is sound very attractive for material processing.

However, there are no published reports on the preparation of CeO_2 and substitution of Ce atoms by other elements via spray freeze drying techniques for catalysis application. Only a few publications were studied the preparation of oxide materials using spray freeze drying method [28-30].

Based on the above-mentioned considerations, this study first deal with the continuous synthesis of pure CeO_2 by spray freeze drying method and study the physico-chemical characteristics of the synthesized materials. Then, synthesis of substituted cerium oxide nano-particles are investigated using two different elements with higher and lower ionic redii (lanthanum and cobalt). Experiments were performed to study the influences of the precursor type and Ce/La ratio on the properties of the final product. Based on the obtained results, protocols are proposed to synthesize Co/Ce-La with controlled compositions.

2. Experimental

2.1. Material preparation

Figure (1) shows a schematic illustration of the main procedures for spray freezing method, which mainly involves three steps: freeze granulation, vacuum drying and heat treatment.

2.1.1. Preparation of ultra-fine Ce_2O_3 powder

The raw material cerium nitrate ($Ce(NO_3)_2.6H_2O$, 99% Fluka) was dissolved in deionized water to get 0.05M solution. Then the aqueous solution was fed into the injector by the dosing pump (solution rate 50ml/h) air carrier was used (flow rate of 50ml/min) to sprayed the solution into the three neck flask containing about 1500ml of liquid nitrogen, resulting in frozen droplets. The frozen droplets were put into the chamber of the freeze-dryer (Tray- Dryer MNL-031-A). The freeze-drying program was set based on the lowest melting point of the solution. So, the frozen droplets were dried at −15°C, 3×10−1 Torr for 45h, and then at −5°C, 1.5×10−1 Torr for 20h. After freeze-drying, the Ce_2O_3 powders were synthesized by calcined the freeze-dried precursor powders at 600oC for 6h in the presence of purified air.

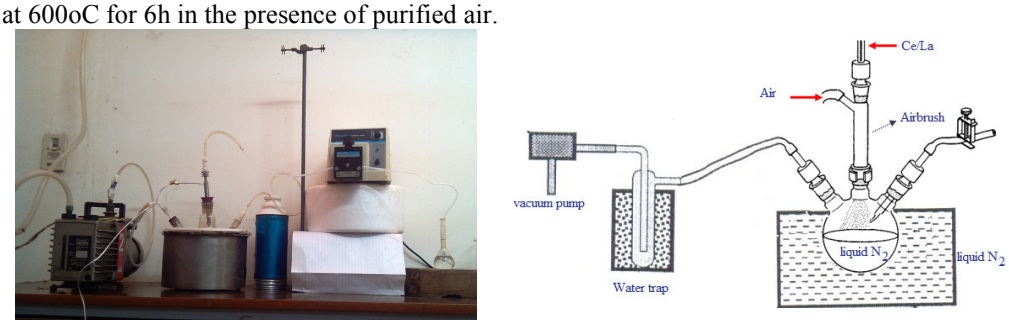

Figure (1): spray freeze drying method

2.1.2. Preparation of Co_2O_3 doping Ce_2O_3 support

Cerium nitrate ($Ce(NO_3)_2.6H_2O$, 99% Fluka) and Cobalt nitrate ($La(NO_3)_3.6H_2O$, 99% Cambrian chemicals) are used. 0.05M ceria/ cobalt solution (Ce/Co= 4) is prepared. The solution is dispersed in liquid nitrogen, and then the frozen droplets were placed in a freeze-dryer for the same above conditions. The samples were calcined at 600°C for 6h.

2.1.3. Preparation of La_2O_3 doping Ce_2O_3 support

Using Cerium nitrate (Ce(NO3)2.6H2O, 99% Fluka) and Lanthnium nitrate (La(NO3)3.6H2O, 99% Cambrian chemicals) as the raw materials. 0.05 M ceria solution with different lanthanam concentrations (Ce:La= 1:0.2, 1:0.5, 1:1, 1:1.5 and 1:2) are prepared. The solutions were dispersed in liquid nitrogen, and then the frozen droplets were placed in a freeze-dryer for the same above condition. The samples were calciened at 600°C for 6h.

2.1.4. Preparation of Co/Ce-La material

A 250ml cobalt nitrate solution was prepared by dissolving $Co(NO_3)_2.6H_2O$ (99% Fluka) in deionized water to get 0.05M concentration. Appropriate amount of the previously prepared CeO_2-La_2O_3 oxide powder was added to the cobalt nitrate solution to get different Co loading (5 & 10wt% of Co), and left for 48h under vigorous stirring. Then the suspensions were sprayed into liquid nitrogen to form frozen droplets. The frozen droplets were put into the chamber of the freeze-dryer. The obtained powders were calcined at 600^{o}C for 6h.

2.2. samples characterization

2.2.1. Thermal gravimetric analysis (TGA)

Was carried out using SETARAM Labsys TG-DSC16 equipment in the temperature range of room temperature up to 1000^{o}C under a nitrogen flow, in order to follow the thermal stability of the prepared samples.

2.2.2. X-ray Diffraction Analysis (XRD)

Was carried out by Shimadzu XD-1 diffractometer using Cu-target& Ni-filtered radiation, to trace the various changes in the crystalline structure and the different phases accompanied preparation method. Sample powders were packed in glass holder, during the measurement of the diffraction intensity with step scanning in 2θ range between 4 and 90^o. The phase identification was made by comparing to the Joint Committee on Powder Diffraction Standards (JCPDS). The crystalline size, D_{XRD} was calculated according to the Scherer equation: $D_{XRD} = 0.9\lambda/B \cos\Theta$, where λ is the wavelength of the radiation, and Θ is the diffraction angle. B is the corrected half-width of the diffraction peak. The reflection from the (1 1 1) plane was used to calculate the crystallite size. The geometrical specific surface area (S_{XRD}) was also determined, assuming spherical particles, according to $S_{XRD} = 6\times10^3/\rho D_{XRD}$, where ρ(g cm^{-3}) is the theoretical density. Scherrer analysis was performed to determine the average crystalline domain size, which was calculated by the Scherrer formula ($D = 0.89\lambda\ \beta \cos\theta$) with the FWHM and a peak position (2θ) of several peaks, where D is the crystallite size, λ is the wavelength of the radiation, β is the corrected peak width at half-maximum intensity, and θ is the peak position. The average value is given as the mean crystallite size.

2.2.3. Temperature programmed reduction (TPR) measurements

Were carried out to investigate the redox properties (the ease of reducibility of the metal oxide) over the resultant materials. The experiments were performed in automatic equipment (ChemBET 3000, Quantachrome). Typically, 100 mg of the pre-calcined sample was loaded into a quartz reactor and pretreated by heating under an inert atmosphere (20 ml min^{-1} N_2) at 200^{o}C for 3h prior to running the TPR experiment, and was then cooled to room temperature in N_2. Then the sample was submitted to a constant rate of heat treatment (10^{o}C min^{-1} up to 1000^{o}C) in a gas flow (80 ml min^{-1}) of the hydrogen/nitrogen (5/95 Vol%) mixture as a reducing gas. A thermal conductivity detector (TCD) was employed to monitor the amount of hydrogen consumption.

2.2.4. High resolution transmission electron microscopy (HRTEM) spectroscopy

Was conducted using a JEOL 2100F TEM at an accelerating voltage of 200 KV. To prepare the TEM samples, a dilute particle–ethanol colloidal mixture was ultra sonicated for 30 min and a drop of the solution was placed on a carbon coated Cu TEM grid.

2.2.5. The textural properties

Were determined from the N_2 adsorption-desorption isotherms measured at liquid nitrogen temperature (-196^{o}C) using NOVA2000 gas sorption analyzer (Quanta Chrome Corporation) system. All samples were degassed at 200^{o}C for 17h in nitrogen atmosphere prior to adsorption to ensure a dry clean surface. The adsorption isotherm was constructed as the volume adsorbed (Vcm^{3}g^{-1}) versus the equilibrium relative pressure P/Po, where P is the equilibrium pressure and Po is the saturated vapor pressure of nitrogen. The BET surface area (S_{BET}) was calculated using the five-point Brunauer–Emmit–Teller (BET) theory. Mean particle size (D_{BET}) was calculated from the BET data according to $DBET = 6/(\rho S_{BET})$.

3. Result and discussion

3.1. Energy dispersive X-ray spectroscopy (EDX)

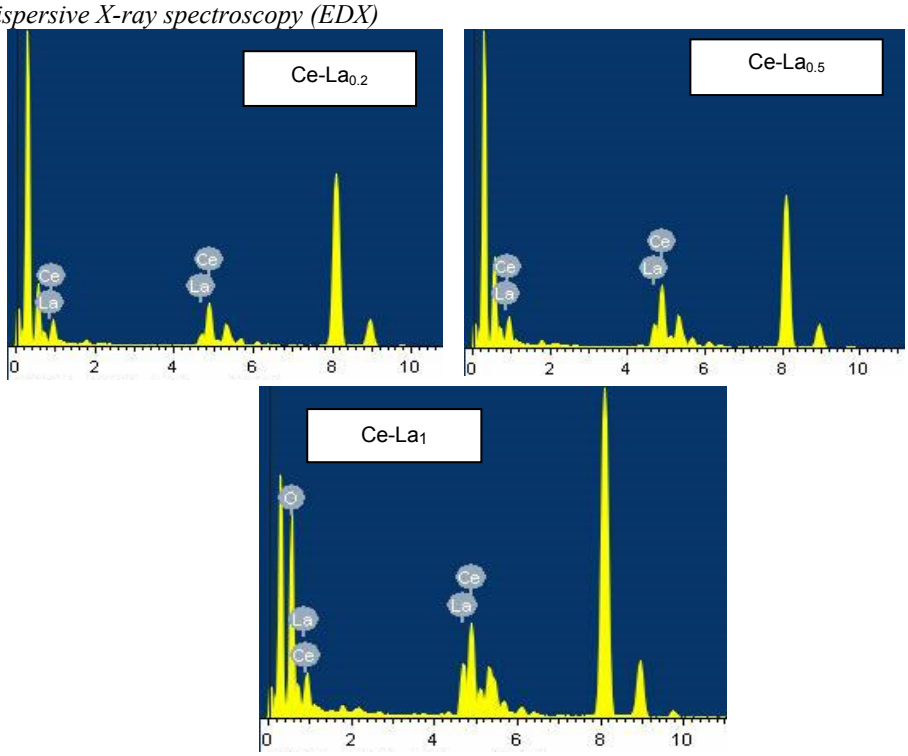

Figure (2): EDX pattern of the prepared Ce-La samples

Energy dispersive X-ray spectroscopy pattern (Fig. 2) of the three Ce-La_X powders was take place to improve the material composition. It is worth to note that, EDX shows elemental analysis of one surface point only, so, the average results of five points were tested and shown in Table 1. EDX elemental mapping (Fig. 2) showed the presence of the cerium, lanthanum and oxygen in all the catalysts, there are peaks at about 1.1, 4.8 keV corresponded to Ce and others around 0.8 and 4.6 keV corresponded to La. As stated before, Ce-La_x oxides were prepared by spray freeze drying method with different Ce:La molar ratio (where, x= 0, 0.2, 0.5 and 1). From Table 1 it can be found that, a mean atomic ratio was obtained in excellent agreement with the nominal composition used in the synthesis step.

Table (1): Ce:La atomic ratio

Element	Atomic%		
	$CeO_2La_{0.2}O_{1.5}$	$CeO_2La_{0.5}O_{1.5}$	$CeO_2LaO_{1.5}$
La	6.32	12.8	19.64
Ce	33.68	27.2	20.36
O	60	60	60
Ce: La atomic ratio	0.188	0.471	0.965

3.2. Thermal gravimetric analysis (TGA)

Thermal gravimetric analysis (TGA) of dried samples was take place in order to choose the correct calcination temperature. The DTA and TGA profiles of prepared CeO_2-CoO_2 and Ce-La_x (x= 0, 0.2, 0.5 and 1) samples from room temperature to 1000°C are illustrated in Fig. 3.

On the TGA curve, the trends of weight change according to the metal incorporated to CeO_2 lattice. Ce-La_x solid solution shows many steps in weight loss compared with CeO_2-CoO_2. for the later one (CeO_2-CoO_2) sample there was a slight decrease (~6wt%) at 60◦C due to adsorbed water on powder, and then a large weight loss (~25wt%) was observed to start at 240°C due to the crystalline water. The total weight loss was 32%.

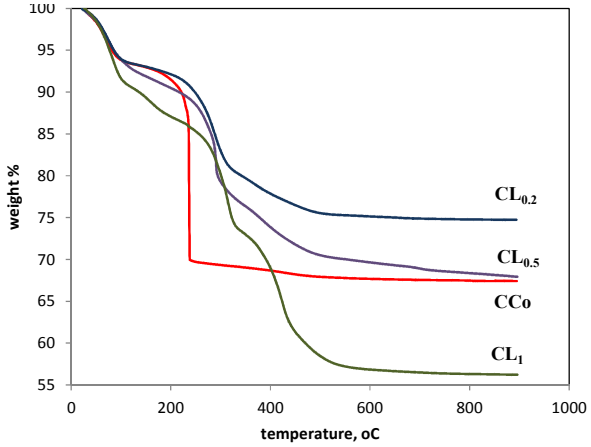

Figure (3): TGA profiles of the prepared samples

While for Ce-La_x samples, from the TGA-DTA analysis shown in Fig. 3, its decomposition was complete at 500°C, so all this samples were calcined at this temperature to reach the stable oxide form. TGA data shows a slight decrease at 100◦C due to adsorbed water on powder, and then a large weight loss was observed about 250°C, then smaller decreasing step at 350°C. The total weight losses were 25.27%, 32.08% and 43.77% for Ce-$La_{0.2}$, Ce-$La_{0.5}$ and Ce-La_1 respectively. The weight loss and the corresponding endothermic reactions suggested the decomposition reactions of the compound or mixture. And the small exothermic peak detected at 300◦C may be due to a crystallization phenomenon and formation of Ce-La solid solution [31]. This can be confirmed by XRD data which indicate the absence of individual oxides, such as La_2O_3 or CeO_2, this is in agreement with the presence of the solid solution between La_2O_3 and CeO_2.

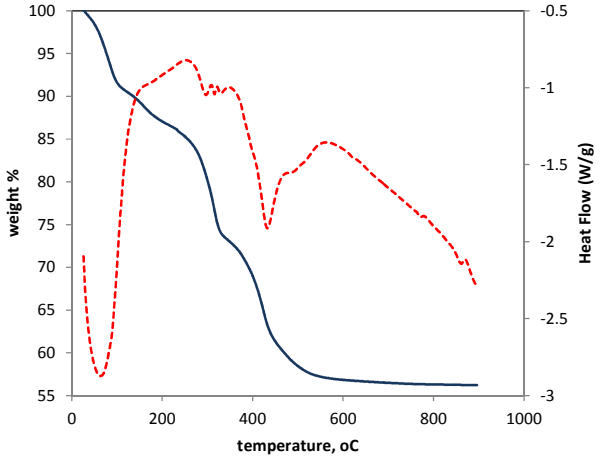

Fig. 4: TGA and DTA profiles of the Ce-La_X sample

We can note that in case in Ce-La_1 sample (Fig. 4), there is an endothermic peak was observed at about 430°C, which can be attributed to the formation of LaOOH from free $La(OH)_3$ present which can't form solid solution with Ce atoms due to high La concentration [32]. This also confirmed by XRD data.

3.3. X-ray diffraction

X-ray diffraction was used to determine the nature of the phases present in the CeO_2, CeO_2-CoO_2, Ce-La_x (Ce:La atomic ratio 1:0.2, 1:0.5 and 1:1) and Co_y/Ce-$La_{0.2}$ (y = 4 and 10) samples (Fig. 5- 7). An interesting observation noted from XRD measurements, peaks are detected corresponding to the typical face centered cubic (fcc) fluorite structure of CeO_2 (JCPDS 00-002-1306) [33-34], however, a detailed analysis of these peaks reveals shift to higher or lower angle side depending on the ionic radius of the dopant cations and also on the Ce:La ratio.

In case of CeO_2-CoO_2 sample (Fig. 5), diffraction peaks are slightly shifted to higher angle side (from 28.507° to 28.5911 for (111) plane), also, the lattice parameters shift to lower value (Table 1). These results indicate that a solid solution of CeO_2-CoO_2 was formed by introducing smaller ionic radius of Co^{4+} (0.54A˚) into the lattice of ceria Ce^{4+} (0.97 A˚). The diffractogram clearly exhibit crystalline features of Co_3O_4 spinel phase (JCPDS 00-043-1003).

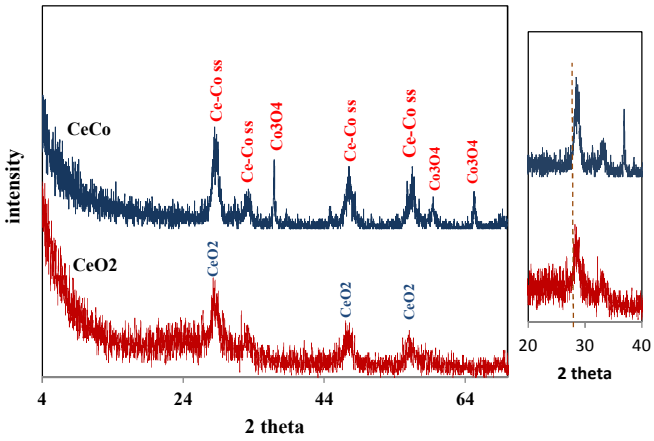

Fig. 5: XRD pattern of fresh CeO_2 and CeO_2CoO_2 samples (ss: solid solution)

On the other hand, XRD pattern of Ce-La_x samples (x=0, 0.2, 0.5 and 1) is represented in Fig. 6. It was found that, as the La content increase, the (111) plane for CeO_2 fluorite structure shift to lower angles (28.507o in CeO_2 shifted into 28.31, 28.09 and 27.4° for Ce-$La_{0.2}$, Ce-$La_{0.5}$ and Ce-La_1 respectively) which is also reflected by an increase in the lattice parameter "a", as reported in Table 1. This shift can be explained as the lattice expansion of CeO_2 and formation of ceria lanthanum solid solutions [35]. The lattice expansion can be attributed to a combination of the effects of increasing number of oxygen vacancies due to La doping, and the larger radius of La^{3+} (1.10 A˚) versus Ce^{4+} (0.97 A˚) which would be consistent with other reports [36]. There are no second phases or additional reflections were found indicating the formation of a single phase (solid solution), except in case of Ce-La_1 sample, in which other lines due to hexagonal close-packed (hcp) structure of La_2O_3 (JCPDS 00-002-0688) were observed.

Interestedly, when we calculated the lattice parameter (a parameter) of the (101) peak (represents La_2O_3 phase) appeared in Ce-La_1 sample, it was found to be 0.420nm which is larger than that of pure La_2O_3 phase. This may be refer to the incorporation of Ce^{4+} (0.97) cation into the La^{3+} (1.10 A˚) cation to form La-CeO_2 solid solution in hexagonal phase structure (larger particle size). Theoretical investigations on mixed $Ce_{1-x}La_xO_{2-x/2}$ oxides, reported by Wilkes et al. [37] have highlighted the partial solubility of CeO_2 and lanthanum oxide. The authors have observed that, at low ionic fraction of lanthanum (x, ranging between $0<x<0.5$), lanthanum dissolved in ceria with lanthanum segregation on its surface occurs; while, at high lanthanum content ($x>0.9$) cerium dissolved in lanthanum with ceria segregation can be predicted [38].

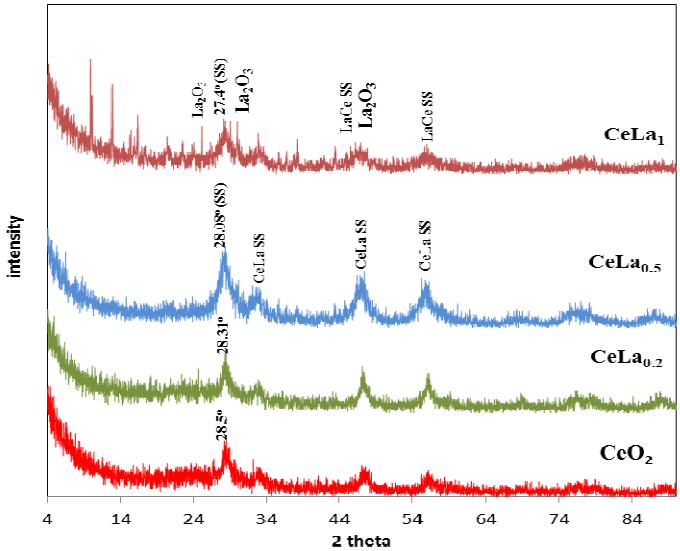

Fig. 6: XRD pattern of $CeLa_x$ samples

XRD patterns of the Co_x/Ce-$La_{0.2}$ (x= 5, 10%) samples impregnated with different Co loadings (Fig. 7), showed peaks corresponding to the cubic fluorite structure of the Ce–$La_{0.2}$ solid solution. No separate CoO phases were found by XRD for Co_5/Ce–$La_{0.2}$, this indicates that the CoO species are finely dispersed on the support beyond the XRD detection limit (< 3 nm). The peak position of Ce–$La_{0.2}$ was invariant with the Co content, and the peak width changed only marginally. At higher Co loading (10%), the diffractogram clearly exhibit crystalline features of Co_3O_4 spinel phase (JCPDS 00-043-1003).

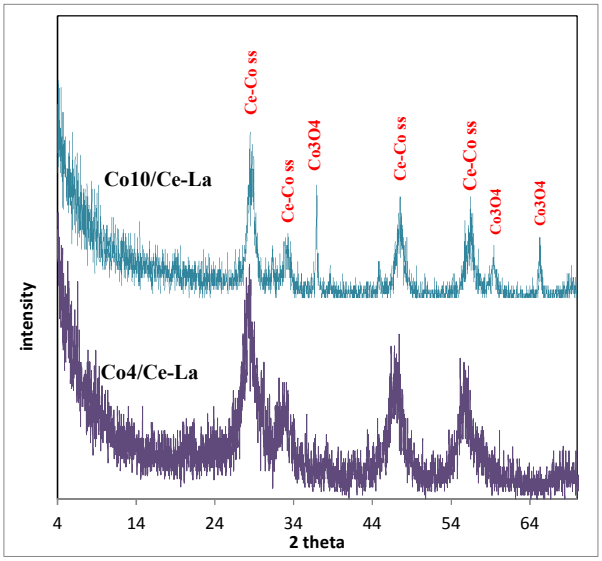

Fig. 7: XRD pattern of $Co_y/CeLa_{0.2}$ samples

In general, the XRD peaks for all samples are quite broad indicated that, the samples prepared by spray freezing method are in nano-size range [39]. The average crystallite size determined by applying the Scherrer equation to the characteristic (111) peak of CeO_2 from the XRD results after structure refinement are listed in Table 2. In comparison to the pure ceria, which had a crystalline size of 11 nm, CeO_2-CoO_2 solid solution exhibited much smaller crystallite sizes. While, Ce-La had larger crystallite sizes which increase by increase of La content. interestingly, the impregnation of Co by spray freeze drying method lead to slightly increase in crystal size.

Table (2): XRD data of the prepared samples

	Phase	D_{XRD}, nm	a, nm	S_{XRD} m^2/gm	D_{BET} nm	d/D_{XRD}
CeO_2	(111) flourite	11.4	0.542	367	47	0.42
CeO_2CoO_2		8.6	0.540	546	60	0.7
$CeO_2La_{0.2}O_{1.5}$		17.1	0.543	211	49	0.29
$CeO_2La_{0.5}O_{1.5}$		18.7	0.545	162	41	0.22
$CeO_2LaO_{1.5}$	(111) flourite	19.3	0.554	130	257	1.35
	(101) hexagonal La_2O_3	41.3	0.420			
$Co_4/Ce\text{-}La_{0.2}$	(111) flourite	17.6	0.543	201	50	0.31
$Co_{10}/Ce\text{-}La_{0.2}$	(111) fluorite + Co_3O_4 spinel phase	18.32	0.543	193	53	0.32

When using the Scherer equation, we assume that the particle size effects are only peak broadening; however, if the particles are non-uniform, the particle size will be under estimated. The mean particle size (D_{BET}) can be obtained from the BET data assuming that the particles are spherical. The calculated D_{BET} values are always bigger than those of the D_{XRD}. This deviation can be explained by a potential presence of small agglomerates and grain boundary interfaces in Ce–cation powders, which are not available to N_2 gas during the BET analysis. Moreover, XRD can detect the sub grains within particles [40]. It is well known that, the ratio d/D_{XRD} is an estimative to the degree of agglomeration of the primary crystallites [41], where "d" is the particle size calculated as $d = 6/(\rho A)$ (ρ is the theoretical density). From Table (1), it was shown that, Co cation slightly increase the particle agglomeration, while, La cation decrease the agglomeration (d/D_{XRD}) except high La content ($Ce\text{-}La_1$), lead to great particle agglomeration [42]. On the other hand, Co/Ce-La0.2 show slightly increase in a agglomeration dgree.

3.3. Raman characterization of mixed oxides

Fig. (8, 9) shows Raman spectra of pure CeO_2, CeO_2-CoO_2 and $Ce\text{-}La_X$ samples with different La ratio. For pure CeO_2, the single sharp band around 461cm^{-1}, ascribed to the Raman F_{2g} mode of CeO_2, as asymmetric breathing mode of the oxygen atoms surrounding each cation, is aband of fluorite structural material [34]. Since only oxygen atoms move, the mode frequency should be nearly independent of the cation mass [44].

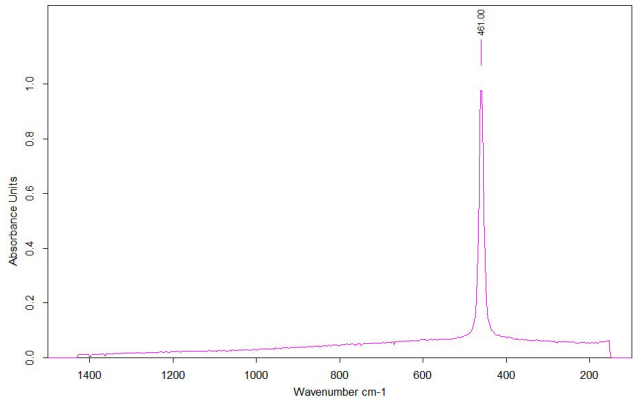

Fig. 8: Raman spectra of pure CeO_2 sample

For Ce–La_X samples with low content of La (0.2, 0.5), a strong band around 458cm^{-1} and 452cm^{-1} respectively is observed, ascribed to the Raman F_{2g} mode of CeO_2 [34]. Moreover, the addition of La into CeO_2, the band shifts to low wave numbers, and its intensity becomes weaker, because the atomic mass of La is larger than that of Ce and the insertion of La ions can decrease the vibration frequency of metal anion bond [45]. Additionally, there appear for four bands,one at 110cm^{-1}, the other two at 590–740cm^{-1}, and the fourth one at 1100cm^{-1}. Mc Brideetal.[46] reported that, band at 590–740cm^{-1}, is linked with the oxygen vacancies in the CeO_2 lattice. The reason for the formation of the band at 590cm^{-1} is that when two Ce^{4+} ions are substituted by two La^{3+} ions, one oxygen vacancy is introduced into the fluorite lattice in order to maintain the electrical neutrality, so as to cause the broad peak on the high frequency side of the F_{2g} band. Thus the band can be linked with lattice defects which result in the creation of oxygen vacancies. It is noted that the changing trend of the intensity for the band at 110cm^{-1} can be correlated with that of the band at 590cm^{-1}, indicating that the band at 110cm^{-1} may be due to the other asymmetric vibration caused by the formation of oxygen vacancies [47]. finally, the band at 1077cm^{-1} can be attributed to $La_2O_2CO_3$ [48]. With the increase of La ratio higher than 0.5, Fig 5b, the concentration of oxygen vacancies decrease, and the action of cations on oxygen vacancies becomes strong, so, the intensity of band at 590–740cm^{-1} decrease. And also the intensity of F_{2g} mode of CeO_2 decrease, which may be attributed the formation of $La(OH)_3$ phase as ascribied by XRD data.

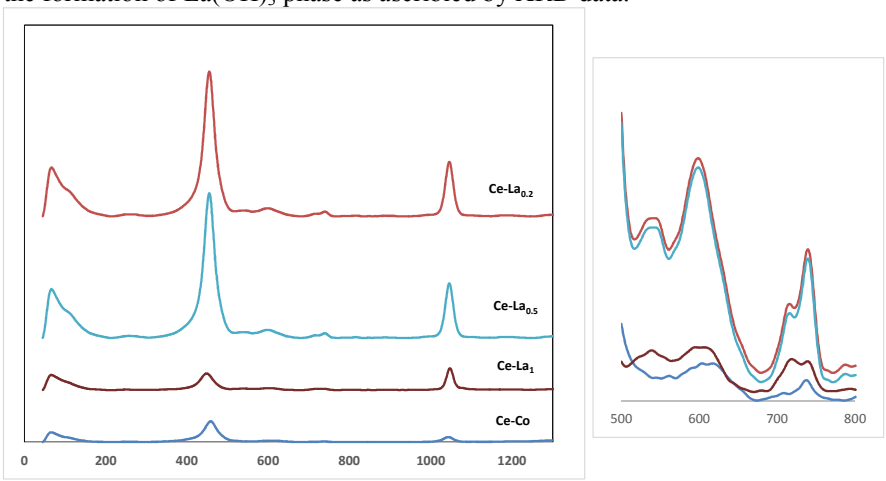

Fig. 9: Raman spectra of the prepared samples

This behavior of Ce-La_X different from that in case of doping ceria with Co cations (Fig. 9), in which the oxygen vacancies are orderly arranged in the solid solutions and the proportion of Ce and Co can be well situated. F_{2g} band shifts to high wave numbers 470 cm^{-1}, and its intensity becomes weaker, because the atomic mass of Co is smaller than that of Ce [49].

3.4. Temperature programmed reduction (TPR)

Temperature programmed reduction of the prepared samples shows reduction profile with the occurrence of two peaks, the small and intense peak located at higher temperature (600^oC) due to bulk reduction of CeO_2. The H_2 uptake at this temperature was decreased by increasing amount of lanthanum, due to the quantities of ceria and hence its oxygen vacancies become increasingly fewer. The second is a high intense peak located at lower

temperature (512°C) due to surface reduction. The doping of ceria with lower valence La^{3+} leads to the introduction of oxygen vacancies that can be expressed by Kröger–Vink notation as:

$$La_2O_3 \xrightarrow{2CeO2} 2La'_{Ce} + 3O_o^x + V_o^{\bullet\bullet}$$

Where La/Ce represents the Ce^{4+} site occupied by La^{3+}. As reported by Zhang et al. [50], the increase addition of La2O3 into CeO2 system would lead to the formation of more oxygen vacancies due to the charge compensation in the material, the vacancies (VO••) with positive charge may attract the doping ions (La/Ce) with negative charge to produce complexes (2 La'_{Ce} $V_O^{\bullet\bullet}$ 2 $La'_{Ce}V_O^{\bullet\bullet}$ La'_{Ce}) due to electrostatic attractions. In accordance, as the La concentration increases the peak at 512oC shift to higher temperature due to increase interaction between Ce and La, this because, at low concentration the VO•• are probably free and easily reducible while at a high level of doping, the defects association near the dopants begin to form [51].

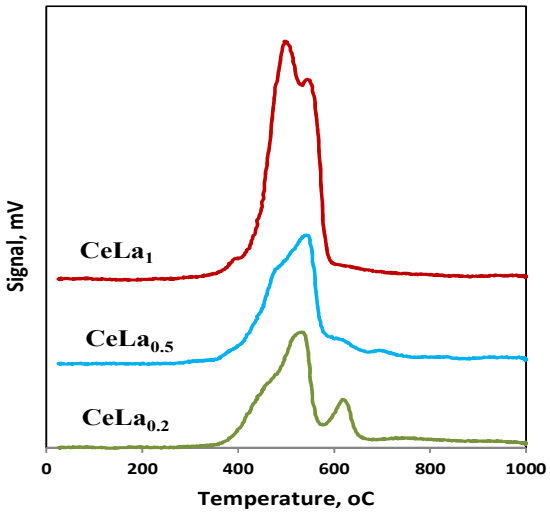

Fig. 10: H_2 consumption profiles during TPR of $CeO_2La_xO_{1.5}$ samples

Moreover, Fig. 10, shows that the lower temperature peak (512°C) is accompanied by a shoulder at about 450°C that can ascribe to the surface oxygen adsorbed on the Ce^{4+} vacancies produced due to the replacement of Ce^{4+} by smaller valence La^{3+}. Further increase in dopant addition causes an increase in the intensity of this shoulder (that becomes a peak at 500°C with shoulder at 530°C in case of Ce-La1). The presence of this new peak at lower temperature (500°C) can confirm a higher Ce^{4+} replacement by La^{3+} ions that promote the diffusion of O^{2-} anion within the lattice, facilitating the bulk and surface reduction at lower temperature [52]. It is well known from XRD analysis, the expansion of CeO_2 lattice due to La^{3+} doping lead to lattice strain and the formation of free volume can facilitate the equilibrium of oxygen atom between the surface and bulk promoting the surface-bulk oxygen transport. This phenomenon is responsible for the observed reduction behavior [53].

3.4. Texture properties (BET surface area):

Specific surface area, pore volume and average pore diameter play an important role espcially in the performance of the materiales as catalyst, adsorpent and supports. The supports must have the properties of larger specific surface area, pore volume and suitable pore diameter. Significant information about the textural properties of the prepared mixed oxides and its metal loading samples were obtained by the analyses of nitrogen adsorption–desorption isotherms (Fig. 11) and collected in Table 3.

Table (3): Textural properties for the prepared samples

	Surface Area m^2/g	S_{XRD} m^2/gm	Pore Volume cc/g	Pore Radius Å	Micro pore volume cc/g	Micro pore area m^2/g	External Surface Area m^2/g
CeO_2	87.8	367	0.086	23.91	0.025	52.59	35.2
CeO_2CoO_2	90.2	546	0.092	10.38	0.016	34.37	43.3
Ce-$La_{0.2}$	74.7	211	0.084	18.45	0.017	36.93	36.7
Ce-$La_{0.5}$	72.3	162	0.062	18.50	0.019	38.27	36.0
Ce-La_1	9.6	130	0.030	11.38	0.000	0.00	9.6
Co_4/Ce-$La_{0.2}$	71.5	201	0.063	14.32	0.013	28.66	35.13
Co_{10}/Ce-$La_{0.2}$	68.3	193	0.055	12.85	0.011	25.72	33.56

Fig (11) shows that, all samples (except Ce-LaO_1 sample) show type II isotherm according to

Brunauer's classification, indicating the adsorption to proceed by unrestricted monolayer-multilayer adsorption on micropore. The inflection point or knee of the isotherm indicates the stage at which monolayer coverage is complete followed by multilayer adsorption. The first part of the isotherm is very pronounced consequently materials present microporosity as confirmed by the t-plot analysis (Fig. 12). The intercept of the t-plot is almost zero for each sample and the surface area due to micropores are comparable to that of the BET surface area which may be indicate that the surface area of all samples are due to micropore. Though the isotherms are type II yet they exhibit closed hysteresis loops with varying closure pressures depending on the incorporated cation and the Ce:La ratio. The occurrence of a hysteresis loop in type II isotherms has been observed with samples having parallel plate pores. On the other hand, Ce-La_1 sample isotherm (Fig. 11) is type II without hysteresis loop (i.e. desorption points lie on the same adsorption isotherm) this may indicate either nonporous structure or the mesoporosity of entire texture. This also confirmed by v-t plot (Fig.12) and data in Table (3). BJH pore size distribution curve (Fig. 12) shows that, the incorporation of another cation into the CeO_2 lattice induces changes in the pore size distribution with a shift to lower pore diameter.

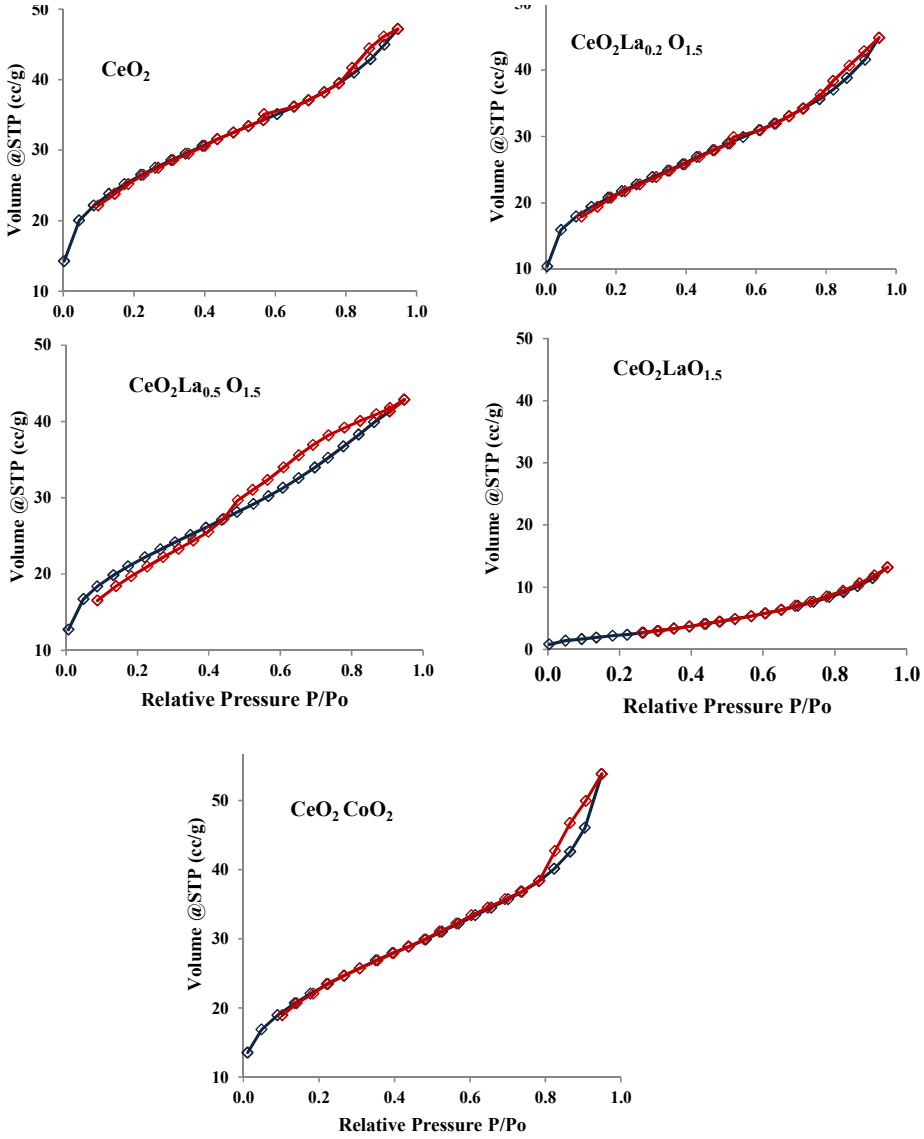

Fig. 11 : N_2 adsorption desorption isotherm of the prepared samples

From data illustrated in Table (3), CeO_2CoO_2 sample showed higher specific surface area than CeO_2. This means that, incorporation of Co^{4+} into the ceria lattice significantly enhanced the surface area of the mixed oxide. Judging from our experimental findings, it is likely that the increase of pore volume is related to the incorporation of CoO_2 ion into the lattice of cubic fluorite structure of CeO_2 makes the lattice more defective, which eventually enhances the mobility of oxygen in the bulk of the CeO_2CoO_2 mixed oxides [54]. On the other hand, the incorporation of trivalent cation (La^{3+}) decrease the specific surface area, which can be confirmed by increase of the crystallite size as shown from XRD data, these results are nearly similar to those recently reported

[55]. The addition of Co over Ce- La_1 using spray freezing method slighity affected texture properties and specific surface area.

The geometrical surface areas (S_{XRD}) of the prepared oxides calculated from XRD data are much higher than that obtained from BET analysis (Table 3). This variation can be related to the fact that S_{XRD} is calculated basing on the diffraction peaks of crystallites with the initial Ce-M_XO_Y solid solution composition, whereas S_{BET} corresponding to all particles in the sample [40]. What is more, solid solution may contain small agglomerates and grain boundary interfaces which are not available to N_2 gas during the BET analysis. We also believe that some internal porosity associated with the grain boundary regions have an influence on the obtained results.

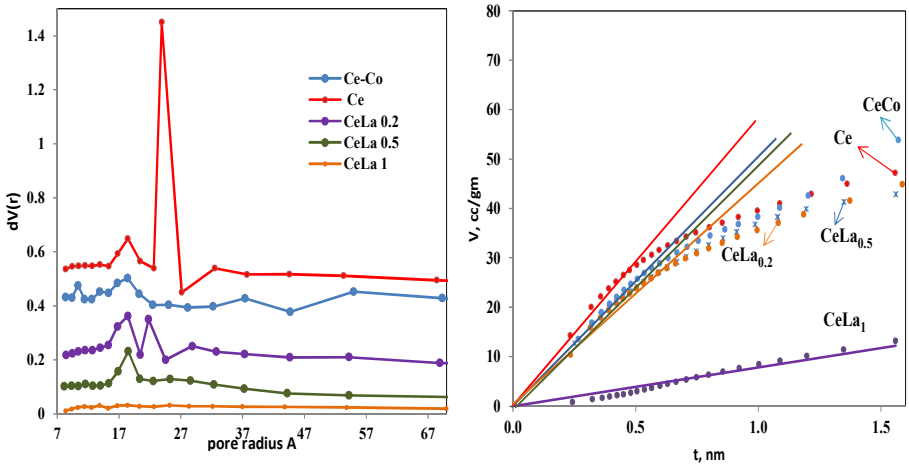

Fig (12): pore size distribution of the prepared samples

3.5. Dynamic light scattering (DLS):

Fig. 13 shows the particle size distribution measured for CeO_2, CeO_2CoO_2 and CeO_2-$La_xO_{1.5}$ (with different Ce:La ratio). The results obtained indicate that the particle sizes of all samples were in nano-scale (in the range of 18-50nm), and the distribution of the powders was well-proportioned, except in case of $CeO_2LaO_{1.5}$ with 1:1 atomic ratio.

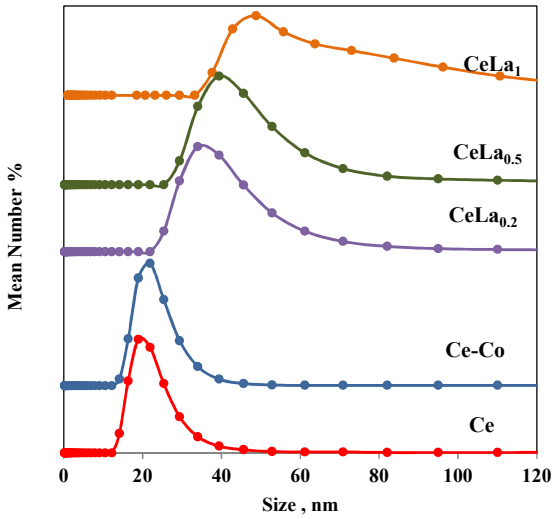

Fig. 13: particle size distribution of the prepared samples

In the process of spray freezing [56], the droplets were sprayed into liquid nitrogen (−196°C). Due to the rapid cooling rate, the chances of nucleation were greatly improved, but the growth rate decreased, resulting in the solute precipitating in the form of ultrafine grained salts. During the rise of temperature (the process when the frozen droplets were taken out of the liquid nitrogen before the first step of freeze drying), the crystal transformation of ice (ice sublimation) resulted in some aggregation of ultrafine grained salts. When the ice sublimated, the ultrafine grain salts turned into precursors, this confirms the broad particle size distribution of all samples.

The incorporation of cobalt onto CeO_2 lattice keep the distribution and particle size as it is. While La

incorporation lead to increase in particle size distribution due to the high atomic radius of La^{3+} than that of Co^{4+} as indicated by XRD data. Also noticeable,, high concentration of La in $CeO_2LaO_{1.5}$ allows some disaggregation of the material showing a non-uniform particle size distribution pattern. This data also confirmed by XRD data.

3.6. Transmission electron microscope (TEM)

HR-TEM images gave us visual impressions of the morphology of the samples. So, TEM investigations, were carried out on freshly prepared samples and reported in Fig. 14, 15, 16. Analysis of these figures showed that, The TEM images of the cerium oxide nanoparticles (Fig. 14), indicate that dense nanoparticles, the overall particle shape was non-spherical and appeared slightly aggregated. The nonspherical shape of particles for the coarse mode may be due to the fact that particles that consist of a single crystal or a large number of crystals will tend to be spheroidal [51].

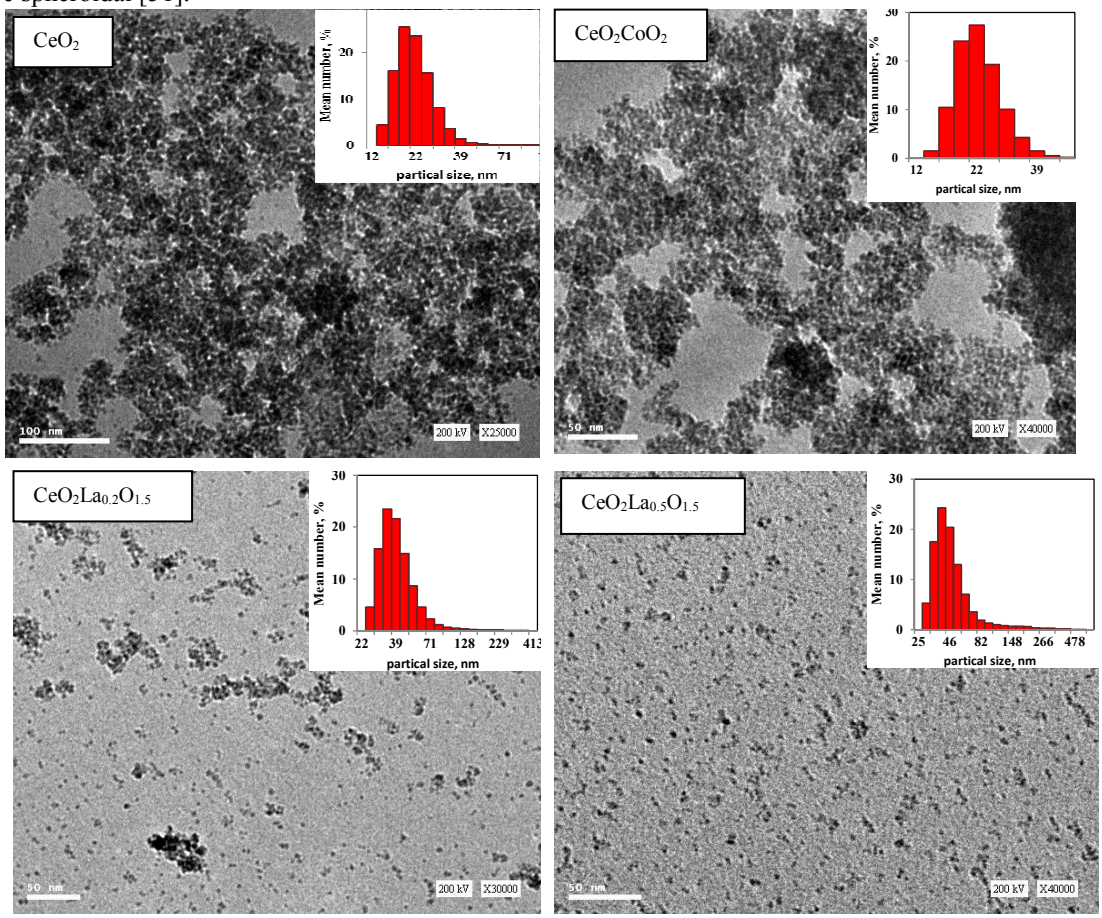

Fig. 14: TEM image of the prepared samples

The incorporation of Co^{4+} in the CeO_2 leads to decrease the particle size and agglomeration degree to some extent. While the incorporation of La^{3+} (Ce: La atomic ratio = 1:0.2 and 1:0.5) lead to formation of a spherical shape particles with increase in particle size and decrease in degree of agglomeration as clearly shown from Fig. (14). On the other hand, Ce-La_1 exhibit very large particle size with high degree of agglomeration (Fig. 15a). And more magnified images of this sample (Fig. 15b), shows another phase was present due to hexagonal close-packed (hcp) structure of La_2O_3, which accorded well with the XRD and DLS data.

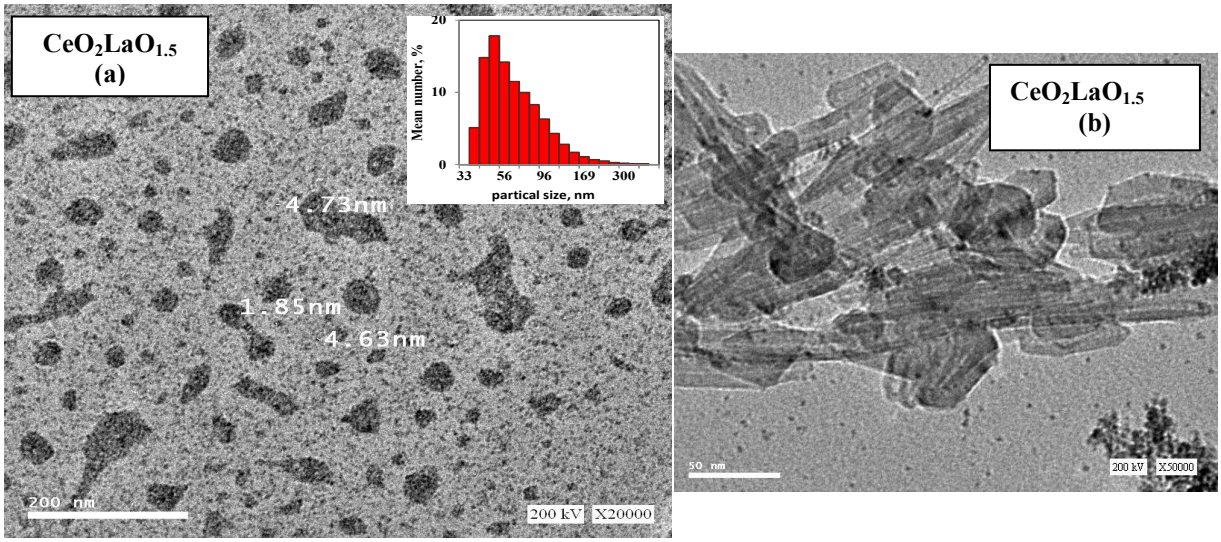

Fig (15): TEM image of the* Ce-La$_1$ *samples

HRTEM images of Co$_y$/Ce-La$_{0.2}$ samples (Fig. 16) confirm the successes of spray freezing method in loading the Co over Ce-La$_{0.2}$ with no effect on the partical siz distribution or agglomeration degree as confirmed by XRD data.

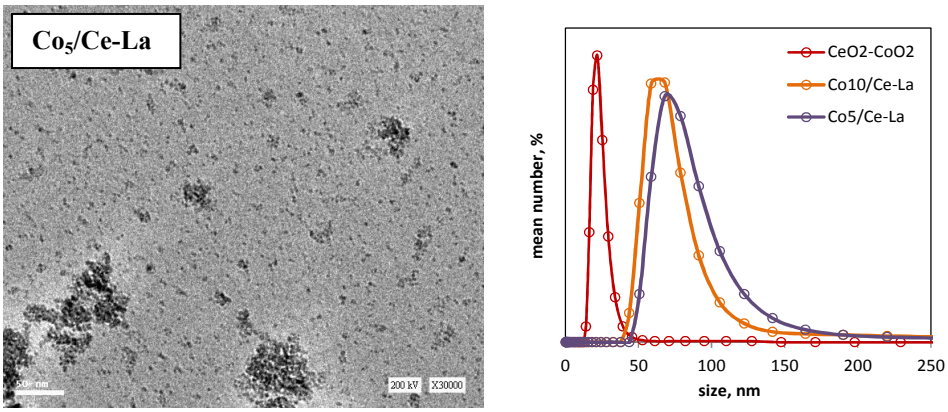

Fig (16): TEM image and DLS pattern of the Co/*Ce-La$_{0.2}$ *sample

Conclusion

To the best of our knowledge, these experiments are the firstreporting the synthesis of CeO_2 substituted with lanthanum (Ce-La$_x$) and cobalet (CeO_2-CoO_2) using a spray freez drying process. From the characterization data of all samples, the advantage of spray-freeze-drying process was successfully achieved. The samples were prepared in uniform and ultra-fine partical size distribution. Aditionally, Co O_3 e frist time to use this process as an impregnation method to loading Co over Ce-La solid solution without marked effect on the structure and texture properties of the support.

References

1. W. Hernandez, O. Laguna, M. Centeno, J. Odriozola: J. Solid State Chemistry 184 (2011) 3014.
2. S. Meher, G. Ranga Rao, Tuning: Journal of Colloid and Interface Science 373 (2012) 46.
3. S. Abdollahzadeh-Ghom, C. Zamani, T. Andreu, M. Epifani, J. Morante: Appl. Catal. B: 108–109 (2011) 32.
4. J.-H. Cho, M. Bass, S. Babu, J. Dowding, W. Self, S. Seal: Journal of Luminescence 132 (2012) 743.
5. G. Renu, V. Divya Rani, S. Nair, K. Subramanian, V.-K. Lakshmanan: Advanced Science Letters 6 (2012) 17.
6. Zhang Q L, Qiu C T, Xu H D, Lin T, Lin Z E, Gong M C, Chen Y Q.: Catal. Today, 175 (2011) 171.
7. V. Ramaswamy, S. Malwadkar, S. Chilukuri: Appl. Catal. B, 84 (2008) 21.
8. L.F. Liotta, G. Di Carlo, G. Pantaleo, A.M. Venezia, G. Deganello: Appl. Catal. B, 66 (2006) 217.
9. Zhang Y, Gong W P.: Min & Metall Eng. 27 (2007) 77.
10. Chen T F, Gong W P, Yang D R.: Min & Metall Eng, 28 (2008) 94.
11. L. Kundakovic, M. Flytzani-Stephanopoulos, J. Catal. 179 (1998) 203.

12. A. Bueno-Lopez, K. Krishna, M. Makkee, J.A. Moulijn, J. Catal. 230 (2005) 237.
13. V. Belliere, G. Joorst, O. Stephan, F.M.F. de Groot, B.M. Weckhuysen, J. Phys. Chem. B 110 (2006) 9984.
14. J.J. Kingsley, L.R. Pedreson, Mater. Lett. 18 (1993) 89.
15. H.M. Zhang, Y. Teraoka, N. Yamazoe, Chem. Lett. (1987) 665.
16. H. Taguchi, H. Yoshioka, M. Nagao, J. Mater. Sci. Lett. 13 (1994) 891.
17. P. Gordes, N. Christiansen, E.J. Jensen, J. Villadsen, J. Mater. Sci. 30 (1995) 1053.
18. S.H. Lee, J.Y. Lee, Y.M. Park, J.H. Wee, K.Y. Lee: Catalysis Today 117 (2006) 376.
19. N.R. Rabbani, P.C. Seville: Journal of Controlled Release 110 (2005) 130.
20. F.K. Roehrig, T.R. Wright: Journal of Vacuum Science and Technology 9 (1972) 1368.
21. K. Oshitaka, I. Toshimichi, Y. Hiroaki, et al.: Japan Journal of Applied Physiology 29 (1990) 1409.
22. L.A. Beyer, C.E. Kalnas: American Ceramic Society Bulletin 66 (1987) 1647.
23. J. Kirchnerova, D.B. Hibbert: Journal of Materials Science 28 (1993) 5800.
24. J. Kirchnerova, D. Klvana: Solid State Ionics 123 (1999) 307.
25. L.X. Li, J.H. Dong, R. Lee: Journal of Colloid and Interface Science 273 (2004) 540.
26. A.B.D. Nandiyanto, F. Iskandar, K. Okuyama: Chemical Engineering Journal 152 (1) (2009) 293.
27. F. Iskandar, I.W. Lenggoro, B. Xia, K. Okuyama: J. Nanoparticle Research 3 (4) (2001) 263.
28. X. Xi, Z. Nie, L. Ma, L. Li, X. Xu, T. Zuo: Powder Technology 226 (2012) 114.
29. S. H. Lee, H.J. Kim, J. W. Nam, H. Jung, S. K. Kang, and K.Y. Lee: Studies in Surface Science and Catalysis, volume 147 (2004).
30. S. H. Lee, J.Y. Lee, Y. M. Park, J.H. Wee, K.Y. Lee: Catalysis Today 117 (2006) 376.
31. Masakuni Ozawa, Ryota Onoe, Hajime Kato: Journal of Alloys and Compounds 408–412 (2006) 556–559.
32. B. Zhang, D. Li, X. Wang, Catal. Today 158 (2010) 348-353.
33. Xue Han, Yunbo Yu, Hong He, Jiaojiao Zhao, Yafei Wang: Journal of Power Sources 238 (2013) 57-64.
34. Reddy BM, Katta L, Thrimurthulu G. : Chem Mater 2010;22:467e75.
35. Xue Han, Yunbo Yu, Hong He, Wenpo Shan: international journal of hydrogen energy 38 (2013) 10293-10304
36. L. Liu, X. Wang, M. Guo, M. Zhang, Journal of Nanoscience and Nanotechnology 11 (2011) 2155–2162
37. M.F. Wilkes, P. Hyden, A.K. Bhattacharya, Appl. Surf. Sci 206 (2003) 12-19
38. GONG Wei-ping, et al/Trans. Nonferrous Met. Soc. China 21(2011) 2671−2676
39. C. Weidenthaler, Nanoscale 3 (2011) 792–810
40. I. Dobrosz-Gómez, M.A. Gómez García, M.I. Szynkowska, I. Kocemba, J.M. Rynkowski: Catalysis Today 191(2012)142–145.
41. M.G. Zimicz, S.A. Larrondo, R.J. Prado, D.G. Lamas: international journal of hydrogen energy 37(2012) 14881-14886
42. Yen-Pei Fu, Shao-Hua Hu, Biing-Lang Liu: Ceramics International 35 (2009) 3005–3011.
43. [29] M.F. Luo, Z.L. Yan, L.Y. Jin, J. Mol. Catal. A: Chem. 260 (2006) 157.
44. [30] V.G. Keramidas, W.B. White, J. Chem. Phys. 59 (1973) 1561.
45. [25] G.Groppi,C.Cristiani,L.Lietti,C.Ramella,M.Valentini,P.Forzatti,Catalysis50 (1999) 399.
46. 46 [34] J.R. McBride, K.C. Hass, B.D. Poindexter, W.H. Weber, J. Appl. Phys. 76 (1994) 2435. [35] R.Q. Long, H.L. Wan, J. Chem. Soc., Faraday Trans. 93 (1997) 355.
47. Catalytic performance of La–Ce–O mixed oxide for combustion of methane" Bo Zhang, Dao Li, Xingyi Wang: Catalysis Today 158 (2010) 348–353
48. E.S. Putna, B. Shereck, R.J. Gorte, Appl. Catal. B: Environ. 17 (1998) 101.
49. M. Kramer, W.F. Maier, Appl. Catal. A: Gen. 302 (2006) 257.
50. Y. Zhang, H. Gu, H. Chen, L. Gao, X. Zhu, L. Guo: Mater. Res. Bull. 44 (2009)775.
51. L.P. Li, G.S. Li, J. Xiang, R.I. Smith, H. Inomata: Chem. Mater. 15 (2003) 889.
52. L. Pino, A. Vita, M. Laganà, V. Recupero: Appl.Catal. B,148–149 (2014) 91.
53. L. Pino, A. Vita, F. Cipitì, M. Laganà, V. Recupero: Applied Catalysis B: Environmental 104 (2011) 64.
54. B.M. Reddy, A. Khan, Y. Yamada, T. Kobayashi, S. Loridant and J.C. Volta, J. Phys. Chem. B 107 (2003) 11475.
55. K.C. Petallidou, A.M. Efstathiou: Appl. Catal. B140 (2013) 333.
56. X. Xi, Z. Nie, Y. Jiang, X. Xu, T. Zuo: Powder Technology 191 (2009) 107.

The IISTE is a pioneer in the Open-Access hosting service and academic event management. The aim of the firm is Accelerating Global Knowledge Sharing.

More information about the firm can be found on the homepage:
http://www.iiste.org

CALL FOR JOURNAL PAPERS

There are more than 30 peer-reviewed academic journals hosted under the hosting platform.

Prospective authors of journals can find the submission instruction on the following page: http://www.iiste.org/journals/ All the journals articles are available online to the readers all over the world without financial, legal, or technical barriers other than those inseparable from gaining access to the internet itself. Paper version of the journals is also available upon request of readers and authors.

MORE RESOURCES

Book publication information: http://www.iiste.org/book/

Academic conference: http://www.iiste.org/conference/upcoming-conferences-call-for-paper/

IISTE Knowledge Sharing Partners

EBSCO, Index Copernicus, Ulrich's Periodicals Directory, JournalTOCS, PKP Open Archives Harvester, Bielefeld Academic Search Engine, Elektronische Zeitschriftenbibliothek EZB, Open J-Gate, OCLC WorldCat, Universe Digtial Library , NewJour, Google Scholar